Schlink, U., **Mohamdeen, A.**, Raabe, A. (2020):
Temporal modes and spatial patterns of urban air temperatures and limitations of heat adaptation
Environ. Modell. Softw. **132** , art. 104773

Temporal modes and spatial patterns of urban air temperatures and limitations of heat adaptation

Uwe Schlink [1], Abdelrhman Mohamdeen [1], Armin Raabe [2]*

[1] *Helmholtz Centre for Environmental Research – UFZ, Dept. of Urban and Environmental Sociology, Permoserstr. 15, 04318 Leipzig, Germany,*
[2] *Institute for Meteorology, University of Leipzig, Stephanstr. 3, 04103 Leipzig, Germany*
uwe.schlink@ufz.de, *A.Mohamdeen@hotmail.com*, *raabe@uni-leipzig.de*

Abstract

A hot-spot region of climate change is the Middle East where temperatures actually have a rising tendency and this will increase in the future. To mitigate the progressing thermal burden urban planning has to develop adaptation measures. On the basis of micrometeorological simulations for a quarter in Cairo we suggest a decomposition of air temperatures into two temporal and two spatial patterns, respectively explaining 97% and 94% of the temperature variability. We find that land-use has a significant impact on the spatial temperature distribution and should be modified for the purpose of heat adaptation. However, just 13% of the spatial temperature patterns are represented by land-use, which is a quite limited impact. Regional weather conditions are the dominant factor for the spatial as well as the temporal development of urban heat.

Key words: urban air temperature; empirical orthogonal functions; EMVI-met; climate change; adaptation

All authors declare no conflict of interest.

* Corresponding author: U. Schlink (uwe.schlink@ufz.de), Helmholtz Centre for Environmental Research – UFZ, Dept. of Urban and Environmental Sociology, Permoserstr. 15, 04318 Leipzig, Germany; Tel.: ++49 341 235 1554, Fax: ++49 341 235 45 1554

1. Introduction

Average global temperatures tend to increase, but regional climatic conditions can develop in very diverse manner, due to differences in land use, feedback processes, atmospheric stability and global circulations. If we in particular consider the exposure to extreme heat, the changes of both regional climate and population have to be taken into account. For example, Liu et al. (2017) found that for the higher emission scenario RCP8.5 the heat exposure for Europe will increase by a factor of four by 2100, while the heat exposure for Africa will be over 118 times greater than it has been historically. Exposure refers to people in the considered region that are subject to potential risks due to heat.

The Middle East and North Africa region has an arid hot desert climate, where precipitation is low (rainfall is only during December-February and primarily over coastal areas) and vegetation scanty (Lelieveld J. et. al. 2016). Already the 4th IPCC Assessment Report (2011) had indicated that temperatures in Africa are projected to rise faster than the global average increase during the 21st century (James and Washington 2013). An amplified warming of the Sahara Desert was observed for 1979-2012 by Cook & Vizy (2015) strengthening the summertime heat low-pressure area associated with subsidence and the low-level Harmattan trade winds during winter.

Lelieveld et al. (2012) predicted likewise that, by the middle of this century, the Middle East and North Africa will become hotspots where days of extreme heat will have doubled since 1970. The authors argue that the expected extremes are of up to 45-50°C; heat waves occur with significantly prolonged durations (Waha et al. 2017). The mean air temperature of Egypt has a positive trend of + 0.017°C /decade (Egypt second climate communication). Confirming a result of Hansen & Sato (2016), such extreme thermal discomfort could jeopardize the existence of the area's 500 million inhabitants. Extreme heat has important consequences for health (Kalkstein & Smoyer, 1993) and society, and might even trigger a "climate exodus" (Lelieveld et al., 2016).

Nevertheless, most people live in cities where, compared to the rural surroundings, the regional thermal conditions are strongly modified. On the other hand, the design of the urban structures offers potential for the implementation of heat adaptation measures (Elnabawi 2015). A modification of building constructions, building materials, green and blue infrastructure, as well as surface sealing can change the energy balance of a city and mitigate the occurrence and effects of local heat. As local heat is the result of regional climate interacting with urban structures, the question arises which part of the temperature variability can be attributed to land use and, therefore, is available for mitigation measures - and which part of temperature variability is due to regional climate and cannot be influenced by a climate-optimized urban development.

The urban microclimate has characteristic temporal and spatial features and the distribution of air temperature T forms patterns that are related to the urban structure. While pattern recognition in atmospheric data is quite common on the global and regional scales, the application of such methods at the urban scale is scarce. The aim of our study is to analyse spatiotemporal temperature patterns, to interpret them in terms of land use, and to suggest strategies for the adaptation to urban heat. For that purpose we consider temperature data generated with micrometeorological simulations of the software ENVI-met (Bruse and Fleer 1998) for an urban quarter in Cairo, Egypt. These data do not have a great many degrees of freedom as they are highly correlated. Empirical orthogonal function (EOF) analysis is applied to reduce the dimensionality of the data and to identify leading patterns. These patterns are interpreted and utilized for recommendations for adaptation to urban heat. We investigate how temporal temperature patterns are related to the radiation balance, how spatial temperature patterns are related to land use, and whether strategies for heat adaptation are limited.

This paper explains the details of our study and provides reasoned interpretations for the patterns of urban heat. It is the first study estimating the maximum feasible percentage of adaptation to urban heat. Moreover we recommend adequate strategies to mitigate urban heat and discuss the limits of urban climate-adaptation. In this sense, the paper casts a new light on the urban potential for climate change adaptation. The study was exemplified for a region that is prone to extreme heat. However the suggested methods are transferrable to urban quarters in any region of the world.

2. Study area

The Helwan university campus (region of Cairo governorate) was specified as study area. Helwan (650,000 inhabitants) is located between the Mokattam heights and the Nile and characterized by residential buildings and heavy industries and located about 24 km south-east of Central Cairo (Fig. 1). Founded in the second part of the 19th century as a spa town due to nearby warm mineral springs, from 1960, the urbanization and industrialization processes have been growing very rapidly in and around Helwan. Between 2008 and 2011 it was the capital of an own governorate, but now it can be considered a suburb of the Cairo metropolitan area.

Helwan has a warm, dry desert climate with more than 330 days of sunshine per year, an annual average temperature of 21.7°C (maximum monthly temperature in June and July is 34.9°C) and 29mm annual precipitation (Koeppen-Geiger climate zone BWh). A previous study (Robaa, 2013) considering the urban climate at five different districts in Cairo during the period (1990–2010) found in Helwan the highest annual average air temperature and the lowest annual values of relative humidity and wind speed compared to the other districts of Cairo. Robba (2013) concluded that these results are due to the strong impact of land use changes.

Figure 1 : Helwan university campus site, (29°52' N, 31°19' E, 40 m a.s.l.; Google Earth and Images)

The Helwan university campus was established in 1975 (planned by the internationally renowned architectural office Skidmore, Owings & Merrill LLP) at an area of ca. 1,400 km² and has been under construction until now. All buildings in the northern part (student dormitories) have the same architectural design (Fig. 1). In the central part there are sport fields, desert landscape and some plants e.g. hedges, trees and palms arranged as 'inner gardens' (Attia, 2018) with the aim to form a bio-climatic zone protected from wind and sun. Buildings in the south (faculties, library and administration areas) are designed differently. Particular features of nearly all buildings are one or more vertically open slots (Fig. 1, right hand side) for ventilation purposes and to improve the thermal comfort. Most of the buildings are surrounded by vegetation. The main streets are sealed with asphalt, while pavements, narrow canyons and some open squares are constructed by varieties of paving stones e.g. concrete, ceramic and granite.

This skilful designed area suggests the question of how this landscape architecture influences the thermal conditions at the campus. The micro-climate results from interactions of atmospheric conditions with local land use and therefore the air temperature is not constant, but characterised by temporal modes and spatial patterns. In the following we identify these modes and patterns and analyse them in terms of their causes and assess the impact of several factors. We hypothesize that (H1) the variability of urban air temperatures can be described by very few temporal modes and spatial patterns, (H2) there are physical explanations for each of the modes/patterns, and (H3) the impact of each mode/pattern can be used to suggest climate change adaptation measures and to assess their effectiveness.

3. Methodology

3.1 ENVI-met model

ENVI-met includes a three-dimensional prognostic flow model (based on the Navier-Stokes equations), simulates the surface-vegetation-air interactions, the production and dissipation of turbulent energy, the short- and long-wave radiation fluxes, as well as the heat exchange of the atmosphere with buildings, roofs and the urban ground. The ENVI-met model was previously considerably advanced (Hutter, 2012; Simon, 2016) and validated resulting in version 4. For example in a residential district in Freiburg, Germany, for a heat wave day the simulations constantly overestimated air temperature T by approximately 0.2 K regardless of different T values (Lee H. et. al. 2016). Such a bias was not observed with ENVI-met simulations in a Sao Paulo study that were comparable with the measurements (Gusson 2016). An application of the old version 3 of ENVI-met for the Helwan campus (Attia S., 2018) demonstrated the potential to investigate possible impacts of the Bioclimatic-Zones Concept in hot arid areas. Elnabawi (2015) discusses for the old version 3 the overall agreement of simulations and measurements and the potential for integrating ENVI-met into urban design processes to better account for microclimate effects.

Assessing the thermal comfort by means of ENVI-met 4 and the bio-meteorological module, (Salata 2016) recommended a twelve-step procedure, including thorough evaluation of model input parameters, consideration of air temperature together with mean radiant temperature and physiologically equivalent temperature, comparison of simulations to experimental data, and utilization of simulation outputs to provide the thermal comfort in urban regions of Cairo. Although many previous attempts utilized the ENVI-met model (Acero & Herranz-Pascual 2015), most of them used outdated versions of ENVI-met (Lee H. et. al. 2016). Our results are based on simulations of ENVI-met version 4.4.4.

3.2 Implementation of the Helwan Campus region in ENVI-met

In our study of the urban quarter Helwan Campus, we used a raster (grid size 4m x 4m) covering an area of 900m x 900m (225 x 225 grid cells plus additional 12 nesting grid cells at each side to avoid boundary effects; Fig. 2). An image from Google Earth has been used to provide a background map for the input of land use components into the model area input file. All roofs are 'flat' (no inclined roof surfaces) and all buildings are assumed to have the same thermal properties (construction materials) and albedo (colours). Out of the total 50.625 cells, 9.127 cells (i.e. 18%) are covered by buildings while 41.498 grid cells are free of buildings. Building heights vary between 3m and 30m.

Simulated vegetation is classified into the three main types grass (14.2% of grid cells), trees (0.3%) and hedges (17.8%); all types have the same short-wave albedo (0.2) and cover natural 'unsealed' soil. Vegetation is located around the open spaces and has a discrete presence around buildings. 67.7% of the area is without vegetation. Soils are categorized into six classes: loamy soil (63.48%), asphalt road (15.48%), sandy soil (12.79%), brick road (6.88%), and concrete pavement (1.36%).

Simulations were made for a period of two days (15th and 16th August 2014, starting midnight 00:00 AM) and stored in time steps of ½ hour. The first day was used as a spin-up for the model and excluded from further analyses, while the second day contained 48 half-hourly spatial distributions of air temperature 1.5m above ground and was utilized for the analysis of temporal and spatial patterns.

Weather data for the initialization of the model were provided from weather underground database for Cairo airport station, (latitude: 30° 7' 19' N and longitude: 31° 24' 20' E, elevation: 75 meters, WMO ID: #62366), which is the closest available meteorological station. Wind speed 10 m above ground was 3.09 m/s (wind direction: NNW, 340 degrees), initial air temperature 30 °C, air humidity 48% and roughness length was selected as 0.1 m. Using atmospheric soundings (http://weather.uwyo.edu/upperair/sounding.html) gathered directly at Helwan observatory #62378 the air humidity at 2500m altitude was 0.6 g water/kg air. The temperature and humidity conditions at the boundary change during the course of the day, for which we utilized hourly meteorological observations (temperature minimum 05:00 hrs and maximum 16:00 hrs local time, humidity vice versa) as input data to calibrate the run of ENVI-met 4.4.4 (so-called 'forcing').

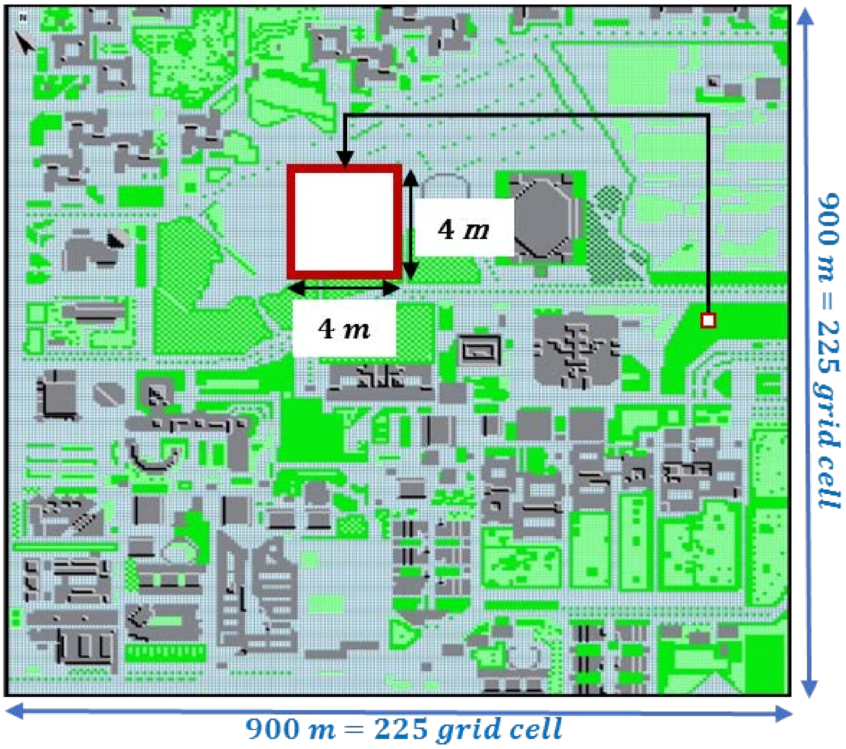

Figure 2: Simulated Helwan quarter has a 4m x 4m raster of calculation and covers an area of 900m x 900m

3.3 Empirical Orthogonal Functions

Empirical Orthogonal Function (EOF) analysis is a commonly used method in multivariate statistics for the analysis of spatial and temporal variability in a dataset (Storch & Zwiers, 2003). EOF aims at the decomposition of a space-time field $T_{t,s}$ $(t = 1,\dots n,\ s = 1,\dots p)$ of air temperature *T*, where *t* and *s* denote time and space positions, into a set of M spatial basis functions $v_s^{(m)}$ (the EOFs) and expansion functions of time $c_t^{(m)}$ according to $T'_{t,s} = \sum_{m=1}^{M} c_t^{(m)}\, v_s^{(m)}$ for the data anomalies $T'_{t,s} = T_{t,s} - \frac{1}{n}\sum_t T_{t,s}$. (1)

This expansion can be realized by eigenvalue or singular value (SVD) decomposition of the covariance matrix

$$Cov(\boldsymbol{T}) = \frac{1}{n-1}\sum_{t=1}^{n} T'^{T}_{s,t}\, T'_{t,s} \ . \quad (2)$$

The covariance matrix is symmetrical and therefore diagonalisable. Assuming there is no perfect multi-collinearity, the covariance matrix is semi definite; hence all its eigenvalues λ_m are positive and λ_m^2 represents the variance of the m[th] eigenvector $v_s^{(m)}$ (Hannachi A. 2007). The percentage of the total variance explained by $v_s^{(m)}$ $(m = 1, \dots M)$ is $(\lambda_m / \sum_{l=1}^{M} \lambda_l) \cdot 100\%$. The eigenvector $v_s^{(m)}$ is also called the m[th] EOF pattern of the anomalies $\boldsymbol{T'}$ and these patterns are sorted in ascending order of the eigenvalues. The set of eigenvectors forms an orthogonal basis in space, i.e., by construction, the EOFs are orthogonal and uncorrelated and provide a complete basis in which the time-varying field can be expanded. The projection of the anomaly field $\boldsymbol{T'}$ onto the m[th] EOF pattern depends on the time point $t = 1,\dots n$, and is given by:

$$\alpha_t^{(m)} = \sum_{s=1}^{p} T'_{t,s} v_s^{(m)} \quad (3)$$

Finally, the decomposition (1) can be written as: $T'_{t,s} = \sum_{m=1}^{M} \lambda_m \alpha_t^{(m)}\, v_s^{(m)}$ (4)

As $rank\big(Cov(\boldsymbol{T})\big) = p$ (if the spatial fields are not perfectly multi-collinear) the EOF analysis will result in $M = p$ patterns, of which the first patterns explain the major part of variance and the contribution of the final patterns can be neglected. An important step of the analysis is the specification of the cut-off for the selection of the most important patterns. For that purpose we will apply the Kaiser-Guttmann criterion. Abandoning patterns of less significance reduces the noise and the degrees of freedom of the data set.

Not every data set is suitable for an EOF analysis. Ill-conditioned data (e.g. random data sets without any mutual correlations) cannot be decomposed into meaningful orthogonal patterns. The **Kaiser-Meyer-Olkin (KMO)** test measures how suitable the data are for an EOF analysis. The higher the KMO value (from 0 to 1) is, the more suitable are the data for EOF analysis. As a rule of thumb KMO=0.8-1.0 indicates that sampling is adequate. KMO<0.6 indicates that remedial action should be taken (Cerny, C.A., & Kaiser, H.F.-1977).

In the current study we considered ENVI-met simulations of air temperature 1.5m above ground for a spatial region of $p = p_1 * p_2 = 225 * 225 = 50{,}625$ grid cells and a period of $n = 48$ half-hourly steps, which results for the field $T_{t,s}$ in a matrix dimension of 48 x 50,625. Our EOF analysis consists of two steps: Firstly, decomposing the data matrix of anomalies $\boldsymbol{T}'$ by EOF we identified characteristic time courses (temporal modes). After removing the diurnal time course from the data ($\boldsymbol{F}'$ is a reconstructed anomalies matrix from the retained temporal modes), we applied the EOF analysis to decompose $\boldsymbol{F}'^T$ into spatial patterns (spatial EOFs). Finally we applied regression analyses to each of these resulting spatial patterns against land use characteristics and atmospheric parameters to gather arguments for the interpretation of the spatial EOFs.

3.4 Analysis on the R- platform

EOF data analysis was made using the ***R***-programming environment and function '***prcomp***' (Venables & Ripley, 2010), which is based on singular value decomposition (SVD) of the centred data sets. After SVD we applied three tests for the selection of most significant EOFs: correlation analysis, Kaiser-Guttman Criterion, and scree plot. Numerical accuracy is higher when analysis is carried out by ***R***'s function-'***prcomp***'. Higher numerical accuracies can be an essential requirement for large data sets like the ones are being investigated here. For regressions we applied the function 'lm', which was extended by hierarchical partitioning (hier.part).

4. Results

4.1 Simulated Air Temperature

The air temperature (T) at 1.5m above ground (Fig. 3) peaks at around 13:00, while the minimum value can be observed at 05:30 hrs local time. Note that the spatial average of T follows a diurnal cycle, shaping from low temperatures in the morning to high values in the afternoon and a temperature decrease in the evening (solid line in Fig. 9). This daily oscillation is a basic feature of temperature records and prior to an analysis of spatial temperature patterns this temporal cycle needs to be removed. For that purpose, in the following we firstly apply the EOF for an identification of temporal variations and removed the daily cycle before the decomposition into spatial patterns by help of a second EOF analysis.

4.2 Temporal modes

The KMO test suggested that the simulated temperatures clearly contain temporal patterns that can be extracted by EOF (KMO=0.94). The decomposition into temporal EOFs resulted in 48 time-series. The first four time-variations are plotted in Fig. 4 (their associated spatial distributions are plotted in the appendix Fig. A1) and we applied three different criteria to select the most important temporal modes.

The first criterion assesses the correlation between the temporal development of spatially averaged air temperatures (Fig. 9) and the temporal modes (Fig. 4). The correlation values are **1.00**, **0.69**, 0.03, -0.006 for mode #1, #2, #3, and #4 respectively (bold values indicate statistical significance at the 95% level). They suggest that most of the variability in time is explained by the first two temporal modes.

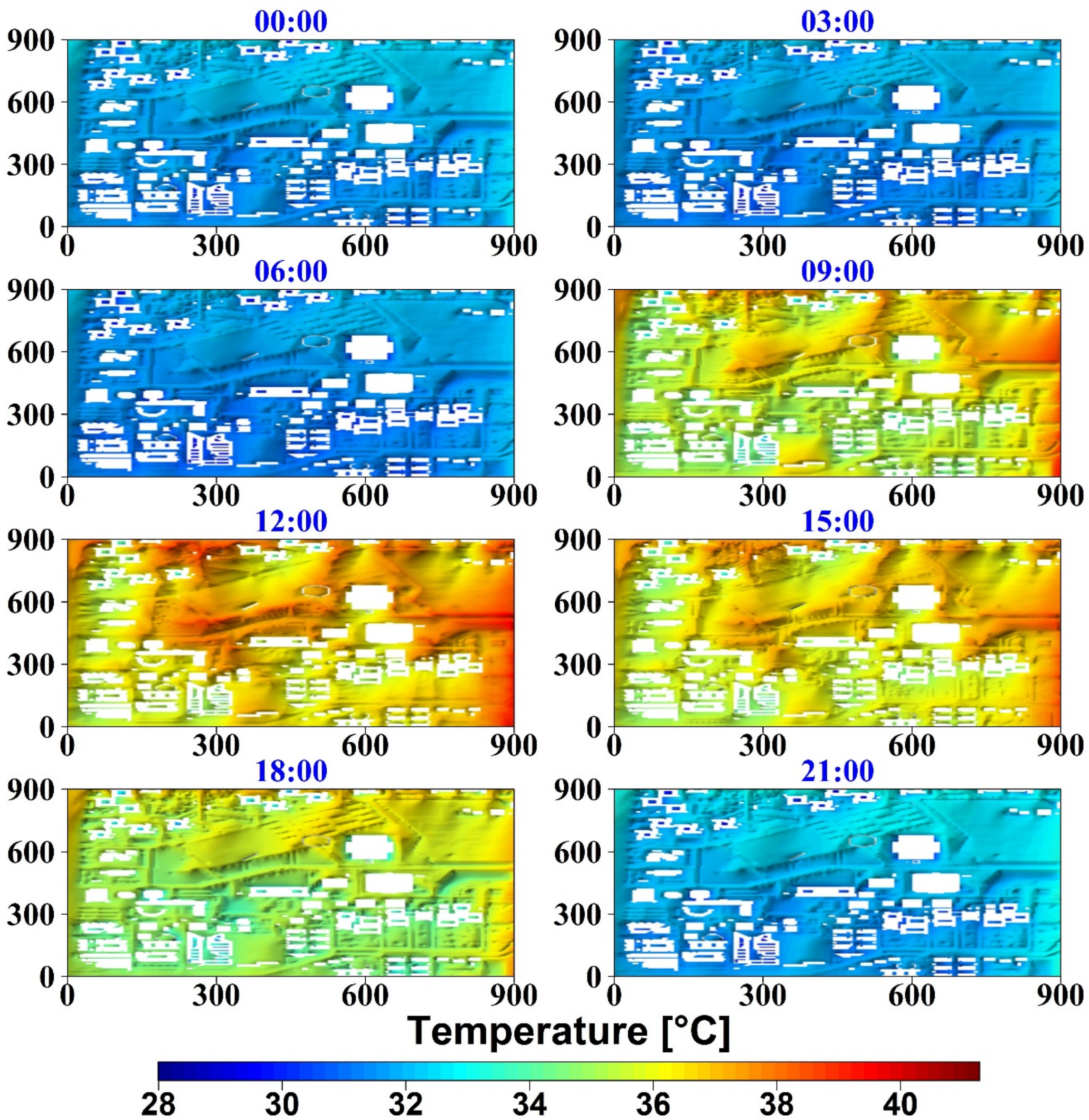

*Figure 3: Time steps of the daily variation of field **T**, the eight images represent the simulated development of air temperature from midnight (top left) until 21 PM (bottom right) on August 16th, 2014. (buildings are represented by white color)*

Secondly, we applied the Kaiser-Guttman criterion (Guttman, 1954) that states that only factors with eigenvalues greater than one (if the variables are standardized, i.e., EOF calculated from the correlation matrix) or greater than the mean of the eigenvalues (if the variables are unstandardized, i.e., EOF calculated from the covariance matrix) are retained and the other eigenvalues are discarded (Fig. 5, left). The first eigenvalue ($\lambda = 30.17$) seems to be separated (much larger) from the rest and explained the maximum variability of the temporal temperature cycles. Only the first two eigenvalues exceed the mean value of 0.86.

A third criterion (D'Agostino & Russell, 2005) considers the explained variance associated with each temporal cycle (Fig. 5, right hand side) and illustrates that the first two temporal cycles explained 73% and 24% of the total variance, respectively.

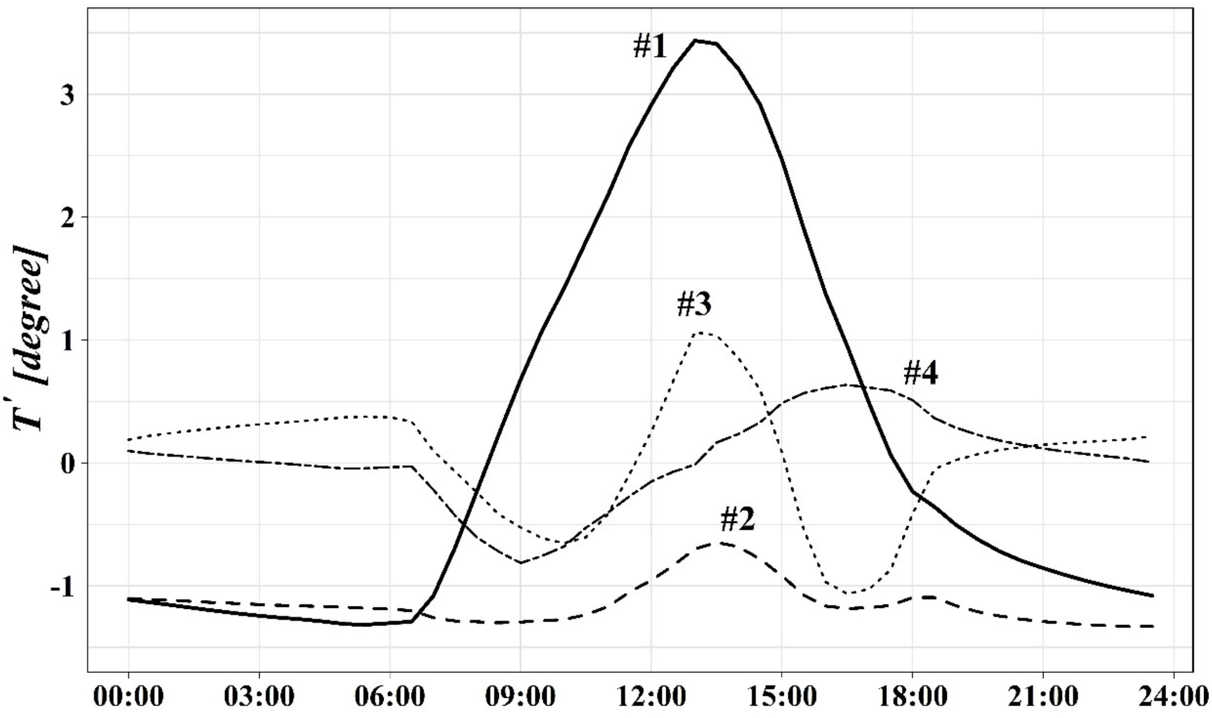

Figure 4: The first four temporal EOF modes (#1-#4) for the temperature anomalies $T' = T - \overline{T}$ *in degrees*

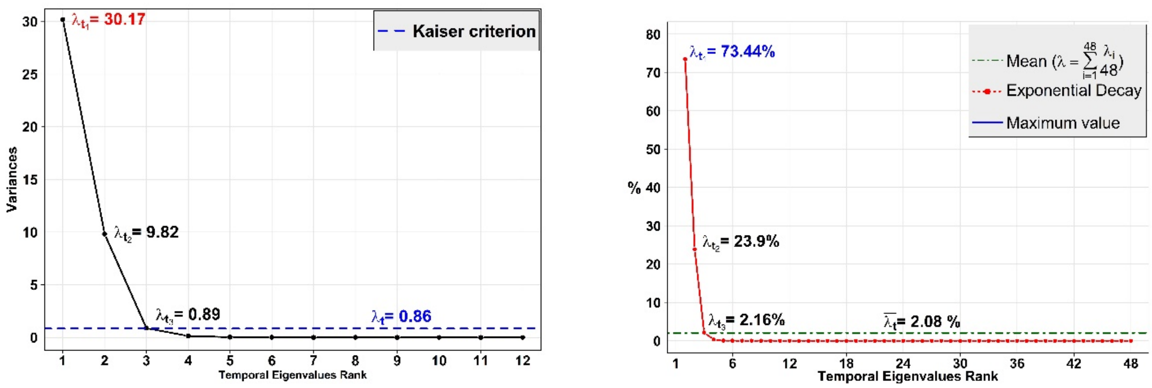

Figure 5: Kaiser-Guttman criterion (left) for the temporal EOFs (dotted line represents mean of eigenvalues) and scree plot (right) of the variance explained by each temporal EOF (exponential decay function fitted).

The most important first two temporal modes represent the daily course of the temperature (cf. Fig. 4). To further analyse only the spatial variations we removed these two cycles from the data (or reconstructed the data from all EOFs except the first two). The resulting half-hourly temperature distributions are called "filtered temperatures" $\boldsymbol{F'}$ and represent only the spatial variability (Fig. 6). Each of these distributions is the anomaly to the daily average temperature of $\overline{T} = 33.64\ °C$. During the course of the day the spatial patterns change in result of different properties of the ground (albedo, heat capacity) as well as due to generated air flows.

While the temporal variability comprised *10-12K* (Fig. 3), the spatial variation of air temperature was in a range of only ca. *2.4K* (Fig. 6).

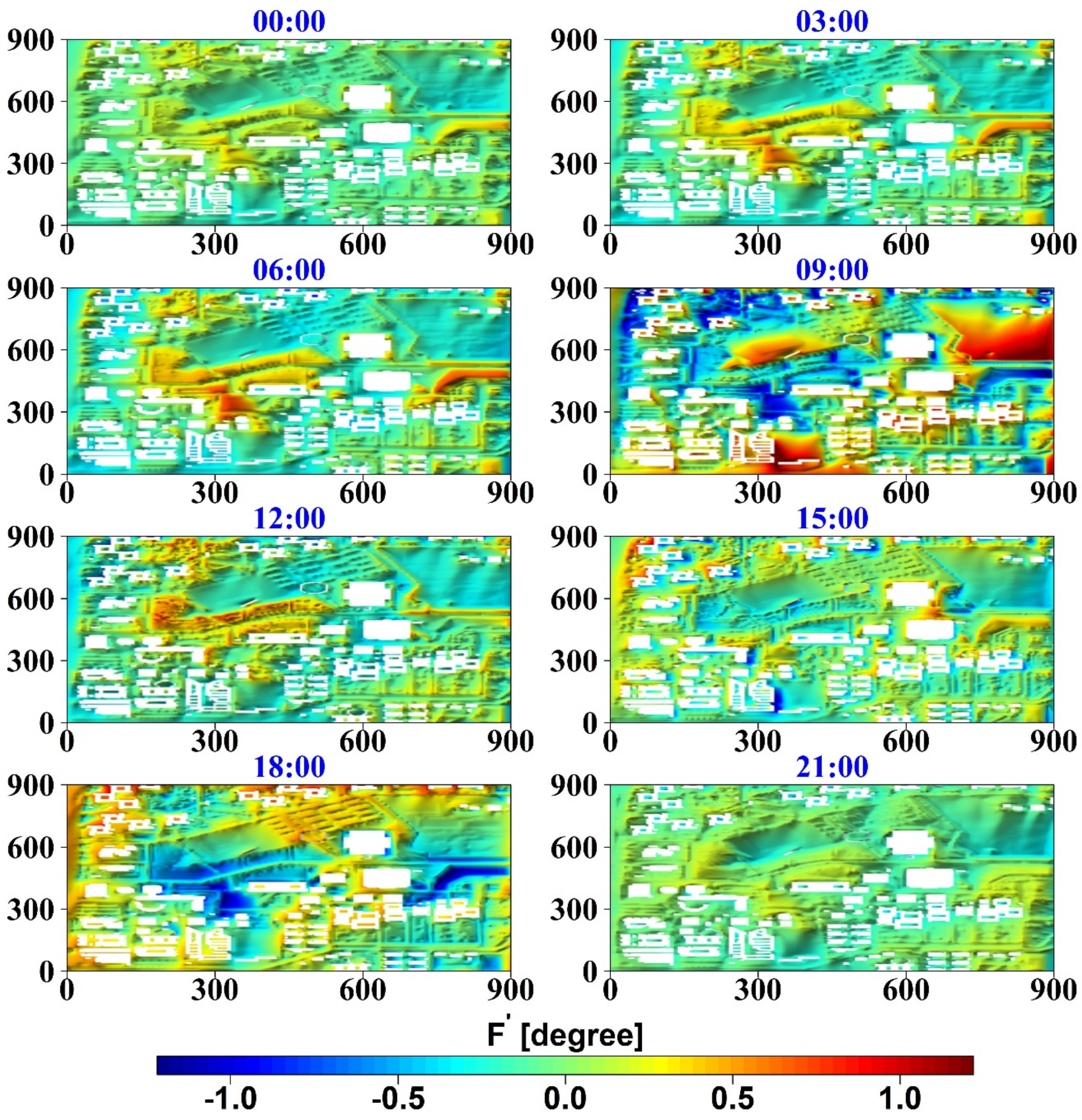

*Figure 6: Spatial distribution of air temperature anomalies at selected time-steps and after omitting the daily temperature cycle. (field **F'** of temperature anomalies).*

4.3 Spatial patterns

For an analysis of spatial patterns of urban air temperatures the EOF technique was applied to the filtered temperature data $\boldsymbol{F'}$ (Fig. 6). From the resulting spatial EOFs (Fig. 7) the magnitude and heterogeneity of the first four patterns is obvious. Considering the associated temporal development of these patterns (Fig. A2), the first three series have the shortest periods of 12 and 24 hours. In particular, the time-series of the second spatial pattern is an oscillation reciprocal to the daily temperature cycle. The time-series of the fourth spatial pattern (Fig. A2) makes more irregular oscillations.

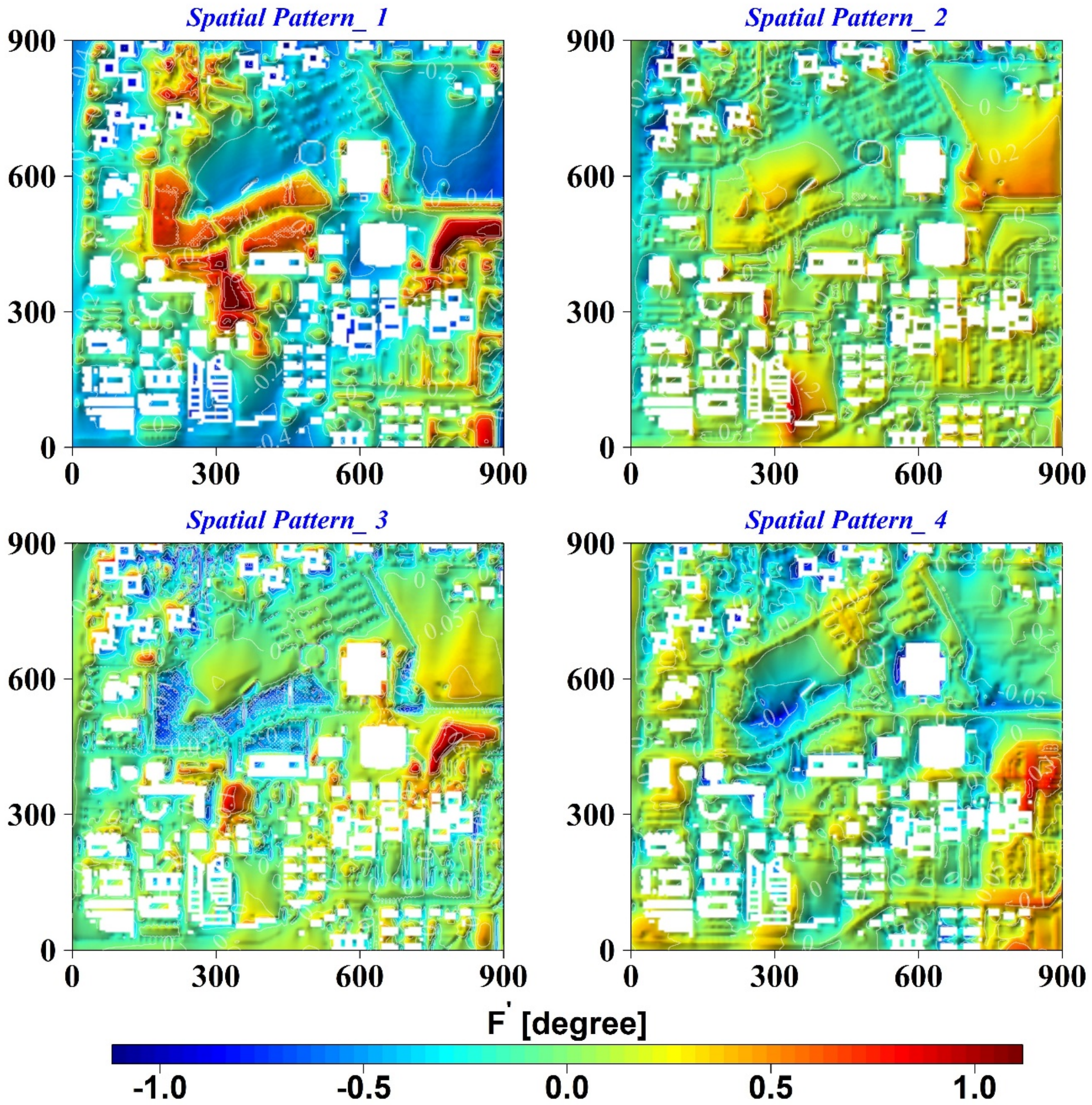

Figure 7: Plots of the first four spatial patterns (EOFs of anomalies to the temperature average of 33.64°C)

To identify the most important spatial patterns we applied a selection strategy similar to that described in section 4.2. A first test was based on the correlation (over 50.625 grid cells) between the identified spatial patterns (EOFs, Fig. 7) and the temperature fields generated by ENVI-met simulations (filtered data $\boldsymbol{F'}$, Fig. 6). For selected time-points (Table 1) we find highest and significant correlations for the first three spatial patterns.

Table 1: Pearson Correlation coefficients between the first four spatial EOFs and the filtered temperature data (F') *at different time points* (***t***)*. Bold marked numbers are significantly different from zero (95% confidence).*

Spatial patterns \ *t*	00:00	06:00	12:00	15:00	20:00
sEOF1	**0.9**	**1.0**	**0.3**	**0.9**	**0.4**
sEOF2	**-0.3**	**0.1**	**0.5**	**-0.3**	**-0.7**
sEOF3	**-0.1**	**0.1**	**-0.7**	**0.3**	**-0.2**
sEOF4	**-0.1**	**-0.2**	**-0.2**	0.0	**0.6**

The Kaiser-criterion for the explained variance of each spatial EOF (Fig. 8, left) indicates that the first eigenvalue($\lambda = 649.9$) is much larger than the remaining. A comparison with the mean eigenvalue $\bar{\lambda}$ suggests that especially the first two spatial patterns are relevant; the third eigenvalue (29.0) is just slightly above $\bar{\lambda} = 24.4$.

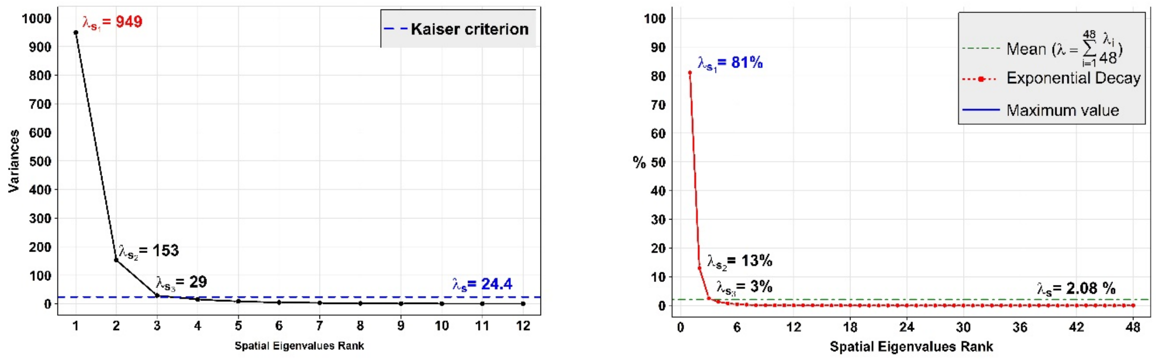

Figure 8: Kaiser-Guttman criterion (left) for the spatial EOFs (dotted line represents mean of eigenvalues) and scree plot (right) of the variance explained by each spatial EOF (exponential decay function fitted).

The scree plot assesses the variance explained by each spatial EOF (Fig. 8, right hand side). The first two spatial patterns explain 81% and 13% of the total variance, respectively (a cumulative contribution of 94%). In result, the first two spatial patterns proved to be most important and they will be discussed in detail in the interpretation section.

5. Interpretation and Discussion

5.1 Simulated air temperature in an urban quarter

Simulated air temperatures *T* have a pronounced variability in space and time (Fig. 3). The latter is dominated by the diurnal cycle (Fig. 9, solid bold line for the area average of simulated air temperatures) as a consequence of the solar heating. In the morning, the incoming short-wave radiation rises rapidly until its maximum at noon and decreases in the afternoon symmetrically to the increase in the morning (Fig. 9, dotted line for the average amount of short-wave radiation in *W/m²*). The short-wave radiation is absorbed by surfaces according to their albedo, resulting in heat-up. As is known from remote sensing, the radiant temperature curve is characteristic for the surface cover (Lillesand, 2015) and determines the output of long-wave radiation (Fig. 9, thin solid line representing an average over the simulated area). Atmospheric gases are relatively good absorbers of long-wave radiation. Together with turbulent heat diffusion this rises the air temperature *T*. Outgoing radiation increases after sunrise but lags somewhat behind the insolation curve; air temperature follows the same pattern that has a 'daily temperature lag' of the maximum behind incoming radiation. The temperature time-series simulated by ENVI-met show a typical daily cycle, indicating that the simulations are plausible (Fig. 9). Air temperature has a minimum at 05:30 and peaks at 13:00, slightly differing from the min/max of forcing (see section 3.2).

Surface warming depends on the material (albedo, heat conductivity, heat capacity) and in this way local warming of air is determined by the structure of the ground (not shown here). This effect can be observed from the air temperature increase in the morning that is very steep for rocks having low heat capacity and conductivity as compared to water, for example. Therefore, air temperature, rates of heating and cooling can often provide significant acquaintance about the conditions and components of the urban land use (e.g. buildings and vegetation and soils). Surface temperatures of buildings normally exceed those of vegetation during the day. The process is conversely during the night, because of the re-radiation of long wave terrestrial irradiance and absence of atmospheric (sun) irradiance. The points where the curves for both vegetation and other components intersect are the 'thermal crossovers'. They indicate times at which no radiant temperature difference exists between two materials and take place shortly after dawn and near sunset. (Lillesand, 2015). At day (night) local warming (cooling) generates baroclinic conditions initiating local air circulations. All these local processes explain the spatial patterns in air temperature (Fig. 3).

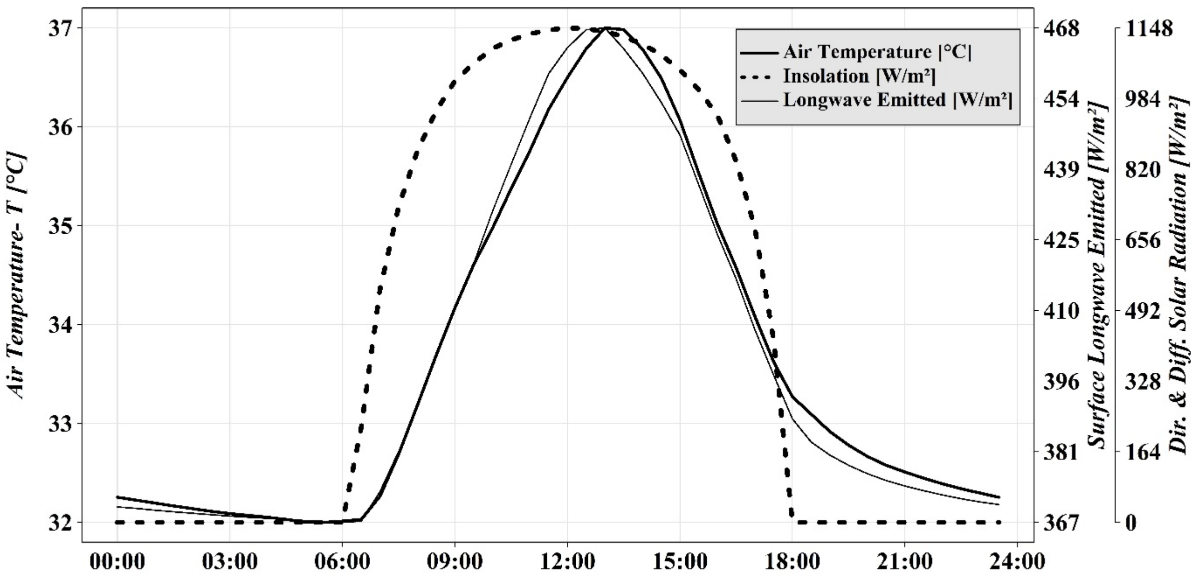

Figure 9: Simulated diurnal air temperature T (solid line), incoming short-wave radiation (insolation, dotted line), and outgoing long-wave radiation (thin line) averaged over the study area (16.08.2014).

5.2 Temporal modes

The first two temporal EOFs characterize the daily temperature cycle. While the first mode (Fig. 4, #1) represents the general daily development of air temperature (compare to *T* in Fig. 9), the second temporal mode has a line curvature that is sharper and associated with a small pronounced protrusion before the trough and after the peak (crest). As the simulated *T* refers to a height of 1.5 m above ground, these protrusions could be due to the shadowing effects of trees, buildings, and some other topographic features. Moreover, the heating strength depends on ground material (see discussion in 5.1) and the orientation of these urban components to the sun change during the course of the day.

The amplitudes of the temporal modes (Fig. 4; *4.75K* for #1 and *1.98K* for #2) correspond to the temporal variability (section 4.2) and result from radiative heating as well as advection of heat that is involved in the ENVI-met 4.4.4 procedure of ‘external forcing’.

Each temporal mode has a spatial representation, the spatial weights (Fig. A1 in appendix). The weights of the first mode exhibit strong positive values in the middle of the domain characterized by trees (cf. Fig. A1, top left, and Fig. A4). This mode accounts for up to 74% of the temporal variance, especially in the region of the largest amplitude. The fraction of local variance explained decreases towards the south and west. The spatial representation of the second temporal mode displays high positive weights at buildings in the south-western area and negative values at a sandy vegetated ground in the North-eastern part. Here the phase of #2 (Fig. 4) is delayed, because in this area the evaporation of moisture produces a slight cooling in the morning in comparison to the temperature rise at build-up areas. This mode explains up to 24% of the variance near its centre of action. The associated time-series consists of a combination of inter-hourly and lower frequency oscillations.

5.3 Spatial patterns

The first two spatial patterns (Fig. 7, spatial pattern 1 with *2.2K* and spatial pattern 2 with *1.5K* amplitude) together explained 94% of the study area’s spatial temperature variability. The temporal development of these spatial patterns is represented by the corresponding time-series (projections in Fig. A2). Both patterns have maximum weight at 09:00, a time when the contrast between warm and cold spots becomes remarkable (see Fig. 6) as a superposition of pattern 1 and pattern 2.

At vegetation spots (Fig. A4), the *T* variability can be qualitatively attributed to the evapotranspiration process in open spaces that is modified by the albedo and emissivity (sand albedo is calculated inside ENVI-met using the soil wetness and the sun zenith angle respectively) of their natural unsealed soils. This was very obvious over sand soil 'sd', roughly most of the zones of high temperature-amplitudes are found to be covered by sandy soil or close to such zones (Coakley, 2003). Positive temperature anomalies are associated to lower evapotranspiration in the off-vegetation region beside the thermal absorption and discharge of the land use structure.

Spatial patterns of air temperature in an urban quarter can be explained by the impact of meteorological and land use parameters. The effects of these factors are studied more in detail by means of regression analyses.

a) *Regression on meteorological parameters*

The first spatial pattern (Fig. 7) clearly represents the field of air temperature anomalies averaged over time $\bar{F}_s{}'$ (with $std(\bar{F}_s{}') = 0.23K$) as can be seen from the fitted regression models $sEOF1_s = 1.02 \cdot \bar{F}_s{}'$, $(R^2 > 0.94)$ and $sEOF2_s = 0.001 \cdot \bar{F}_s{}'$, $(R^2 < 0.07)$. This perfect agreement of sEOF1 (and poor fit of sEOF2) with average temperature anomalies suggests that sEOF1 (but not sEOF2) is determined by atmospheric conditions. In a more detailed analysis we considered meteorological parameters (Fig. 10), including (time averages of) wind speed (ws in m/s), specific humidity (sh in g/kg), turbulent kinetic energy (tke in m²/s²) and long wave radiation emitted from the surface (lwre in W/m²). In the fitted regression models

$$sEOF1_s = 0.6K - 0.14\left(\frac{Ks}{m}\right) \cdot ws_s + 3.56\left(\frac{Kkg}{g}\right) \cdot sh_s - 0.60\left(\frac{Ks^2}{m^2}\right) \cdot tke_s + 0.73\left(\frac{Km^2}{W}\right) \cdot lwre_s \qquad (5)$$

with $R^2 = 0.84$ and

$$sEOF2_s = 0.3K + 0.13\left(\frac{Ks}{m}\right) \cdot ws_s + 0.91\left(\frac{Kkg}{g}\right) \cdot sh_s + 0.06\left(\frac{Ks^2}{m^2}\right) \cdot tke_s - 0.47\left(\frac{Km^2}{W}\right) \cdot lwre_s \qquad (6)$$

with $R^2 = 0.09$, all impact factors are statistically significant (95% level). Along the buildings, long-wave radiation and tke are important (Fig. 10, c+d), in the open regions the wind plays an important role (Fig. 10, a), while the specific humidity (Fig. 10, b) is large in a vegetated sandy region (Fig. A4) in the north-eastern part of the quarter.

As a result of these regressions we clearly identify sEOF1 as the pattern that mostly (at 84%) represents the meteorological conditions of the urban quarter. The impact of meteorology on the second spatial pattern is just 13%, which means that most of this pattern's variability is explained by other parameters. This is studied by help of land use regressions in the following section.

b) *Regression on land use parameters*

The anthropogenic impact on spatial patterns of air temperature is investigated by means of land use regressions (Table 2). We included the three main vegetation types grass, trees, and hedges, as well as five soil classes including; asphalt road, pavement (concrete), loamy soil, sandy soil, and brick road. A regression analysis was applied to identify the most important impact factors for the spatial air temperature patterns. This regression comprises just land use parameters (Tab. 2), but not all details of the physical parameterizations (including surface albedo and soil moisture memory) that are integrated in the soil-atmosphere processes of a grid model (Merrifield, 2016) such as ENVI-met.

In result the urban land use parameters alone explained 41% (Table 2) and the atmospheric parameters alone explained 84% of sEOF1 (eq. 5) by multi-linear regression models. In contrast, the coefficient of determination for sEOF2 was 19% (Table 2) for land use, and just 9% (eq. 6) for atmospheric parameters (considering all factors together in one model explains 85% of sEOF1 and 27% of sEOF2, see Table A1). Interactions of atmospheric and urban parameters did not have any significant effects. We observed that vegetation components have an inverse impact as compared to soil components (Table A1).

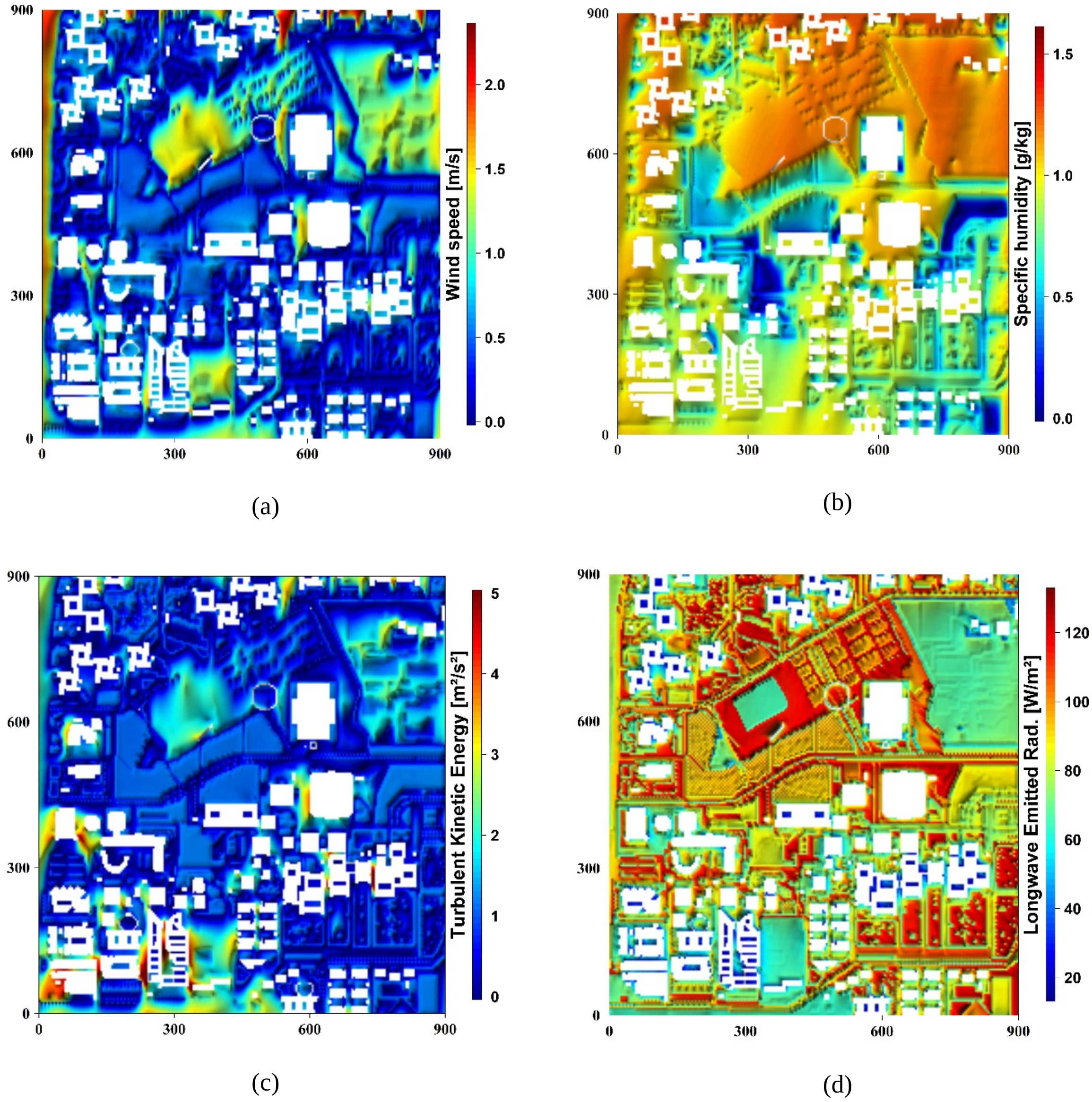

Figure 10: Spatial presentation of daily mean values of selected atmospheric parameters:
(a) Wind speed [m/s], (b) Specific humidity [g/kg].
(c) Turbulent kinetic energy [m²/s²], (d) Surface emitted long wave radiation [W/m²].

The results suggest that *sEOF1* represents the natural variability of the meteorological parameters (either the effect of average temperature, R^2=94%, or the effects of the atmospheric parameters ws, sh, tke and lwre, R^2=84%), while sEOF2 represents the variability due to land use.

A much clearer separation of the impact of both groups of factors results from a hierarchical partitioning analysis, which determines the relative importance of each independent factor and makes the results more directly comparable (Chevan & Sutherland, 1991). Hierarchical partitioning clearly supports the dominant impact of atmospheric parameters on sEOF1 and land use on sEOF2 (Table A2).

Table 2: Multivariate regression models for the first two spatial patters of air temperature anomalies.

Model	***sEOF1***		***sEOF2***	
term	estimate	p.value	estimate	p.value
(Intercept)	-0.367	< 0.001	-0.008	0.748
Trees	-0.010	0.591	0.053	< 0.001
Grass	-0.169	< 0.001	0.019	< 0.001
Hedges	-0.396	< 0.001	0.011	< 0.001
Loamy Soil	0.446	< 0.001	0.003	0.916
Sandy Soil	0.659	< 0.001	0.144	< 0.001
Asphalt	0.463	< 0.001	-0.084	0.001
Bricks Pavement	0.421	< 0.001	-0.045	0.070
Concrete Pavement	0.593	< 0.001	-0.120	< 0.001
R^2	0.41		0.19	

6. Conclusions and Outlook

We conclude that the land use-atmospheric coupling feedback is responsible for urban spatiotemporal patterns of air temperature 1.5m above ground. In our study this was exemplified for the campus of Helwan University and demonstrated that:

- the first temporal EOF represents the typical daily temperature cycle and explains ca. 81% of the daily temperature variation,
- the second EOF explains 24% of the daily temperature variation and characterizes modifications due to land use components, such as buildings and associated shading effects,
- the first spatial pattern (*sEOF1*) nearly equals the mean spatial temperature distribution. Hierarchical partitioning analysis (Table A2) demonstrates that atmospheric parameters, including wind speed, specific humidity, turbulent kinetic energy, and long wave radiation environment account for 68% of sEOF1 and 32% are influenced by land use,
- the second spatial pattern (*sEOF2*) can be interpreted as the effect of land use, because 73% of *sEOF2* is influenced by land use components, including different buildings, neighbourhood, vegetation and soils (and 27% are allocated to atmospheric parameters).

The occurrence of patterns confirms the strong correlation of urban atmospheric data. Our analysis demonstrates that the elimination of the daily cycle is needed prior to the recognition of spatial patterns. In result, 97% of the temporal variations are explained by the identified two daily cycles and 94% of the spatial variability is explained by the two identified spatial patterns. The high representativeness of these four patterns suggests that they are essential for the spatiotemporal distribution of air temperature in the urban quarter (confirming hypothesis H1) and they can be utilized for the recommendation of adaptation measures.

Our investigation ascertained that the temporal modes as well as sEOF1 depend on the prevailing weather situation. Only the second spatial pattern (sEOF2) can be influenced by land use changes (confirming H2). In general, vegetation (grass, hedges, and trees) is conducive to reduced temperatures. Any sealing pavement (asphalt, bricks, concrete) acts to increase the temperature (H3). However the effectiveness of land use changes to mitigate temperature burden is limited, because the pattern sEOF2 accounts for just 13% of the temperature variability.

As the suggested decomposition of urban temperature distributions into patters was exemplified here for an urban quarter in a hot and arid clime that is, moreover, a hot-spot region of climate change, the impact of the weather situation might be stronger compared to other regions in the world. Further studies might demonstrate how the effectiveness of adaptation measures can change with the climate zone.

While the presented approach assesses the amount of temperature variability attributed to land-use changes, a direct prediction of the temperature change resulting from a specific adaptation measure would be desirable. For that purpose an approach for the decomposition of surface temperature values was recently developed (Hertel & Schlink, 2019). This technique might be extended to urban air temperatures in future research work. Both techniques (attribution of temperature variability as well as of temperature increments) could be a useful tool for planners optimizing adaptation measures.

In general physical patterns tend to be non-orthogonal (Hannachi, 2007). A limitation of the EOF analysis is the assumption of orthogonal patterns, because these patterns might result from a superposition of different physical phenomena (Dommenget and Latif, 2002). On the other hand it might be possible that an individual EOF does not represent the effect of a specific atmosphere-land coupling parameter on the air temperature (Roundy, 2014). For example, in our study grass vegetation has a significant impact on both spatial temperature patterns (Table A1).

7. Software and technical notes

For micrometeorological simulations the model ENVI-met version 4.4.4 (science license, http://www.envi-met.com/) was used together with the visualization program LEONARDO. Input data are retrieved from a google.earth image of Helwan University campus, from the weather underground database for Cairo airport station, (latitude: 30° 7' 19’ N and longitude: 31° 24' 20’ E, elevation: 75 meters, WMO ID: #62366), and from the atmospheric soundings website at University of Wyoming (http://weather.uwyo.edu/upperair/sounding.html). Visualisation, conversion of ENVI-met output data (from binary format), and the EOF analysis were done with programs developed in R (R Core Team, 2015, https://www.r-project.org/). Hierarchical partitioning was calculated using the ‘hier.part’ package (Walsh & Mac Nally, 2020)

Acknowledgements: The work was partly supported by the Helmholtz-Climate-Initiative (HI-CAM), funded by the Helmholtz Associations Initiative and Networking Fund. The authors are responsible for the content of this publication.

8. References

1. Acero, J. A. and Herranz-Pascual, K. (2015) ‘A comparison of thermal comfort conditions in four urban spaces by means of measurements and modelling techniques’, Building and Environment 93, 245–257.
2. Attia Shady (2018), THE BIOCLIMATIC-ZONES CONCEPT: LANDSCAPE DESIGN STRATEGY FOR SITE PLANNING IN HOT ARID CLIMATES, Tokyo. https://orbi.uliege.be/handle/2268/167560
3. Bruse M, Fleer H. (1998) Simulating surface-plant-air interactions inside urban environments with a three dimensional numerical model. Environmental Modelling & Software 13, 373-384.
4. Chevan, A., Sutherland, M. (1991) Hierarchical Partitioning. The American Statistician. 45. 90-96. 10.1080/00031305.1991.10475776.
5. Cerny, B. A. and Kaiser, H. F. (1977) A Study Of A Measure Of Sampling Adequacy For Factor-Analytic Correlation Matrices, Multivariate behavioral research 12(1), 43–47.
6. Coakley, J. A. (2003) Reflectance and albedo, surface. Encyclopedia of Atmospheric Sciences, 1914-1923.
7. Cook, K. H. and Vizy, E. K. (2015) Detection and analysis of an amplifying warming of the Sahara desert. Journal of Climate 28, 6560-6580.
8. D'Agostino, R. B. and Russell, H. K. (2005) Scree Test, in Armitage, P. and Colton, T. (eds) Encyclopedia of Biostatistics, Chichester, UK, John Wiley & Sons, Ltd, p. 245.
9. Dommenget, D. and Latif, M. (2002) A cautionary note on the interpretation of EOFs. Journal of Climate 15(2), 216-225.
10. Elnabawi, M. H., Hamza, N. and Dudek, S. (2015) Numerical modelling evaluation for the microclimate of an outdoor urban form in Cairo, Egypt, HBRC Journal 11(2), 246–251.
11. Gusson, C. S. and Duarte, D. H.S. (2016) ‘Effects of Built Density and Urban Morphology on Urban Microclimate - Calibration of the Model ENVI-met V4 for the Subtropical Sao Paulo, Brazil’, Procedia Engineering, vol. 169, pp. 2–10.
12. Guttman, L. (1954) ‘Some necessary conditions for common-factor analysis’, Psychometrika, vol. 19, no. 2, pp. 149–161.
13. Hannachi, A., Jolliffe, I. T. and Stephenson, D. B. (2007) ‘Empirical orthogonal functions and related techniques in atmospheric science: A review’, International Journal of Climatology, vol. 27, no.9, pp. 1119–1152.
14. Hansen, J. and Sato, M. (2016) Regional climate change and national responsibilities. Environmental Research Letters 11, 034009.
15. Hertel D, Schlink U (2019) Decomposition of urban temperatures for targeted climate change adaptation. Environmental Modelling & Software 113, 20-28. https://doi.org/10.1016/j.envsoft.2018.11.015

16. Huttner, S. (2012) Further development and application of the 3D microclimate simulation ENVI-met, dissertation thesis, Mainz University, 137 p.
17. James R, Washington R. (2013) Changes in African temperature and precipitation associated with degrees of global warming. Climatic Change 117:859-872.
18. Kalkstein, L. S. and Smoyer, K. E. (1993) 'The impact of climate change on human health: Some international implications', Experientia, vol. 49, no. 11, pp. 969–979.
19. Lee, H., Mayer, H. and Chen, L. (2016) 'Contribution of trees and grasslands to the mitigation of human heat stress in a residential district of Freiburg, Southwest Germany', Landscape and Urban Planning, vol. 148, pp. 37–50.
20. Lelieveld, J., Proestos, Y., Hadjinicolaou, P., Tanarhte, M., Tyrlis, E., Zittis, G. (2016) Strongly increasing heat extremes in the Middle East and North Africa (MENA) in the 21st century. Climatic Change 137, 245-260.
21. Lelieveld, J., Hadjinicolaou, P., Kostopoulou, E., Chenoweth, J., El Maayar, M., Giannakopoulos, C., Hannides, C., Lange, M. A., Tanarhte, M., Tyrlis, E. and Xoplaki, E. (2012) 'Climate change and impacts in the Eastern Mediterranean and the Middle East', Climatic change, vol. 114, 3-4, pp. 667–687.
22. Lillesand, T. M., Kiefer, R. W. and Chipman, J. W. (2015) Remote sensing and image interpretation, 5th edn, New York, Great Britain, Wiley.
23. Liu, Z., Anderson, B., Yan, K., Dong, W., Liao, H., Shi, P. (2017) Global and regional changes in exposure to extreme heat and the relative contributions of climate and population change. Scientific Reports 7, 43909.
24. Robaa, S. M. (2013) 'Some aspects of the urban climates of Greater Cairo Region, Egypt', International Journal of Climatology, vol. 33, no. 15, pp. 3206–3216.
25. Roundy, P. E. (2014) 'On the Interpretation of EOF Analysis of ENSO, Atmospheric Kelvin Waves, and the MJO', Journal of Climate, vol. 28, no. 3, pp. 1148–1165.
26. Salata, F., Golasi, I., Lieto Vollaro, R. de and Lieto Vollaro, A. de (2016) 'Urban microclimate and outdoor thermal comfort. A proper procedure to fit ENVI-met simulation outputs to experimental data', Sustainable Cities and Society, vol. 26, pp. 318–343.
27. Simon, H. (2016) Modeling urban microclimate: development, implementation and evaluation of new and improved calculation methods for the urban microclimate model ENVI-met, dissertation thesis, Mainz University, 218 p.
28. Storch and Francis W. Zwiers 'Statistical Analysis in Climate Research'.
29. Venables, W. N. and Ripley, B. D. (2010) Modern Applied Statistics with S, 4th edn, New York, Springer.
30. Waha K, Krummenauer L, Adams S, Aich V, Baarsch F, Coumou D, et al. 2017. Climate change impacts in the middle east and northern africa (mena) region and their implications for vulnerable population groups. Regional Environmental Change 17:1623-1638.
31. Walsh, C., Mac Nally, R. (2020) R Package Hierarchical Partitioning, https://cran.r-project.org/web/packages/hier.part/hier.part.pdf

Appendix

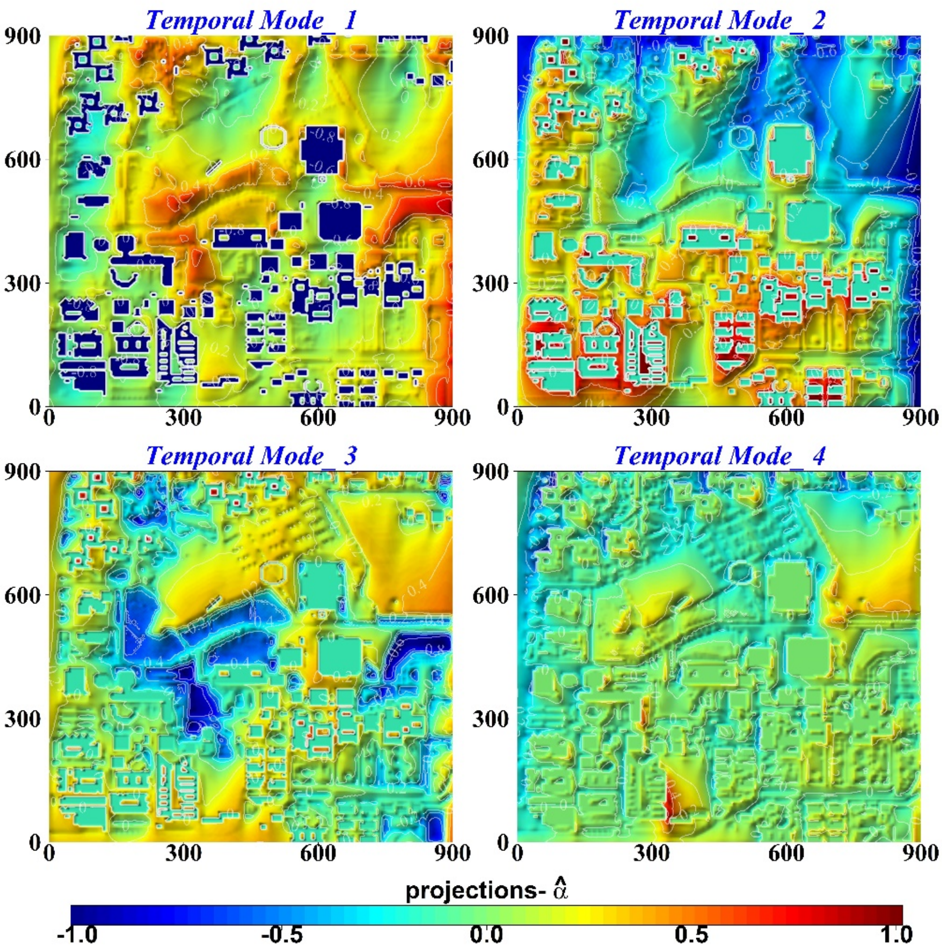

Figure A1: Spatial presentation of the projections (α) of the first four temporal EOFs on the 16th August 2014

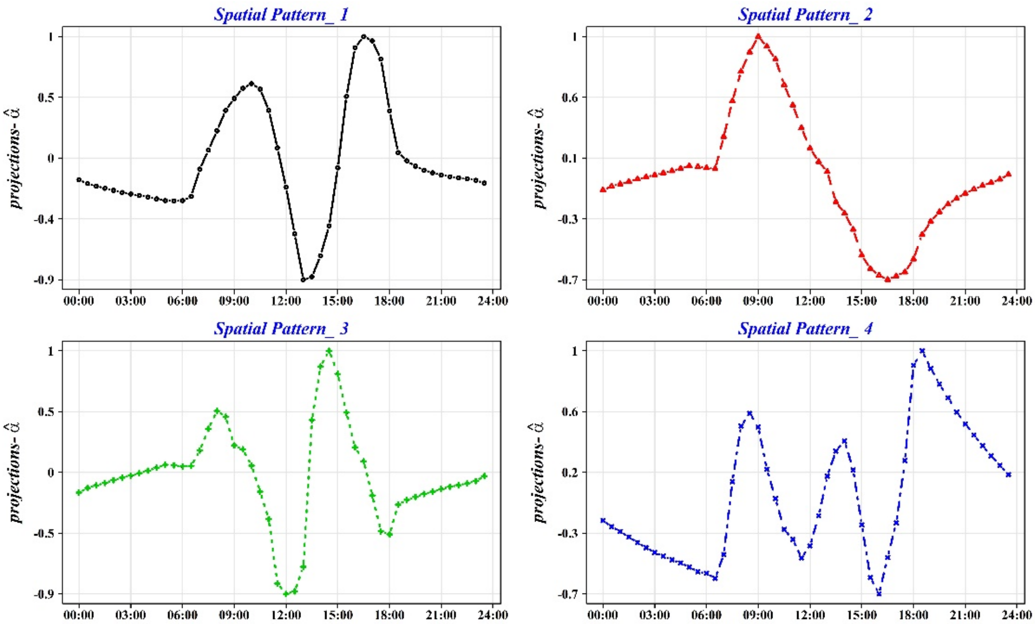

Figure A2: Time-series of the (normalized) projections (α) for the first four spatial EOFs

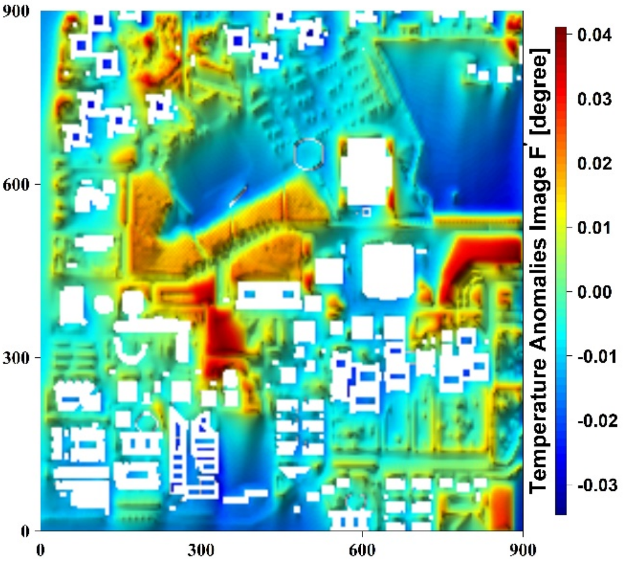

Figure A3: Spatial presentation of the mean temperature anomalies over Helwan- Campus in [K]

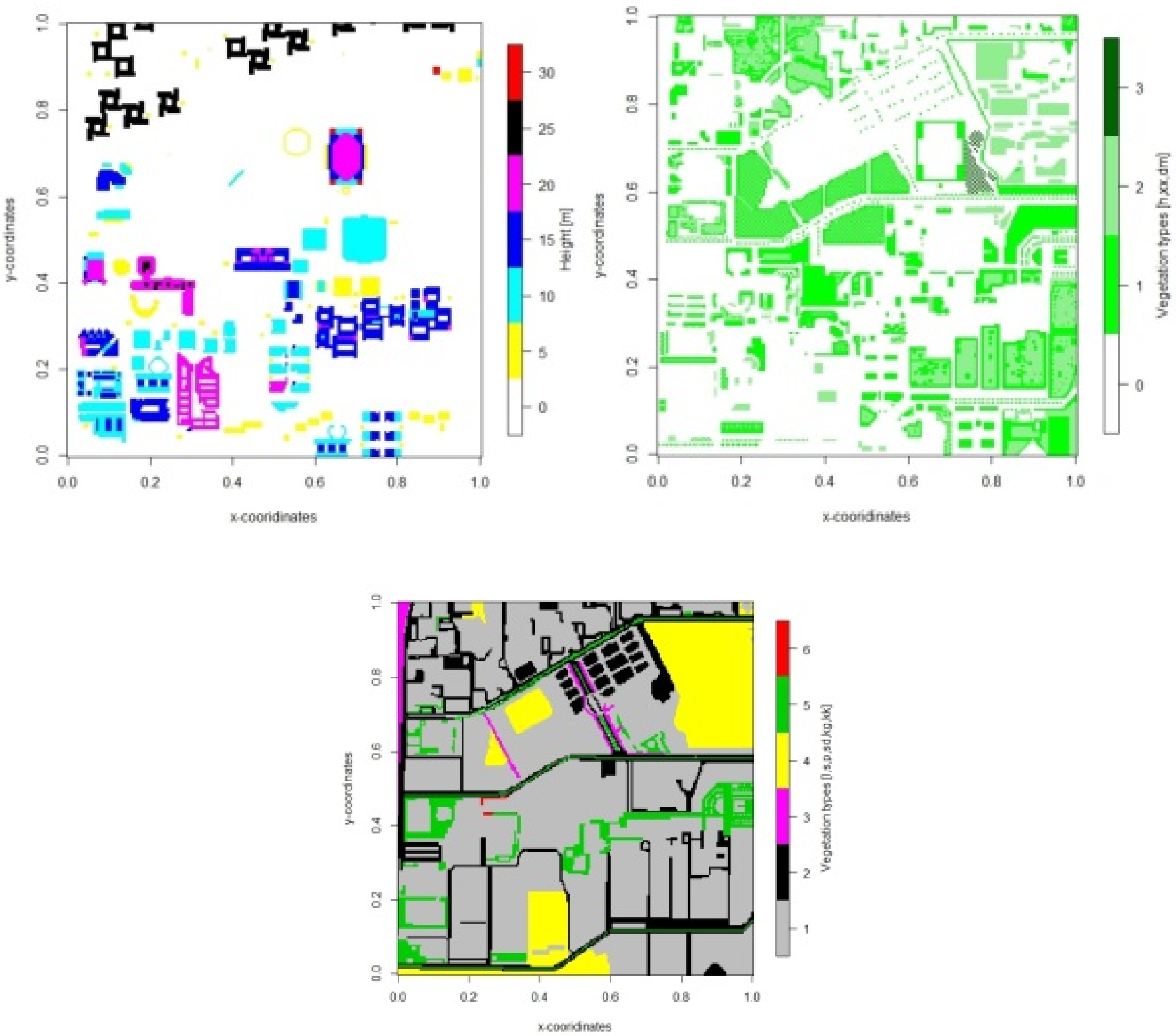

*Figure A4: Soils Map dimensions (900*900 m), the coloured legend indicates different types (loam= l, asphalt= s, pavement= p, sand= sd, yellow stones pavement= kg and red stones pavement= kk)*

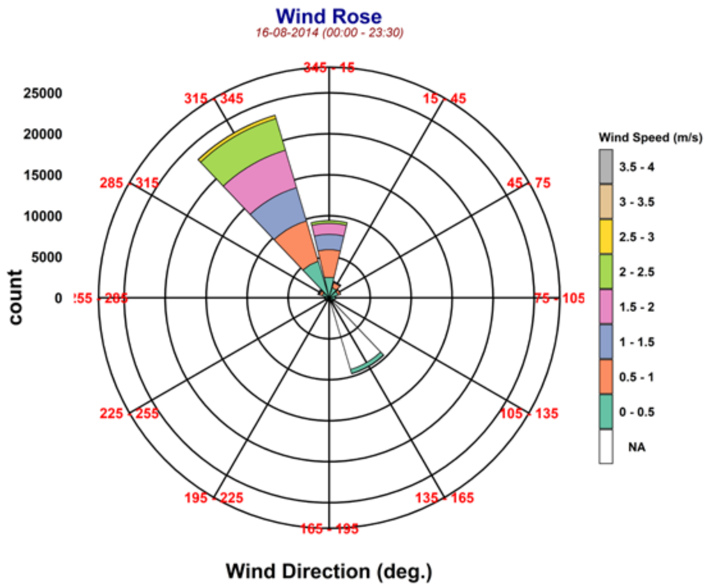

Figure A5: Wind rose, illustrating the frequencies of wind speed and direction at average human height 1.5m in Helwan Campus

*Table A1: Multivariate regression models of the first two spatial patters (**sEOF1** and **sEOF2**) vs. both atmospheric parameters & land use components*

Model Formula	*sEOF1~ ws + sh + tke + lwre+ dm + xx + h + l + sd + s + kg + p*		*sEOF2~ ws + sh + tke + lwre+ dm + xx + h + l + sd + s + kg + p*	
term	estimate	p.value	estimate	p.value
(Intercept)	0.581	<0.01	0.215	<0.01
wind speed (ws)	-0.065	<0.01	0.061	<0.01
specific humidity (sh)	-3.479	<0.01	1.066	<0.01
turbulent kinetic energy (tke)	0.512	<0.01	0.050	<0.01
long-wave radiation (lwre)	-1.200	<0.01	-0.194	<0.01
Trees (dm, 0.3%)	-0.087	<0.01	0.066	<0.01
Grass (xx, 14.2%)	-0.006	<0.01	0.016	<0.01
Hedges (h, 17.8%)	-0.056	<0.01	-0.052	<0.01
Loamy Soil (l, 63.5%)	0.098	<0.01	0.066	0.005
Sandy Soil (sd, 12.8%)	0.021	0.270	0.205	<0.01
Asphalt (s, 15.5%)	0.081	<0.01	-0.016	0.483
Yellow Bricks (kg, 6.8%)	0.021	0.268	-0.005	0.821
Concrete Pavement (p, 1.4%)	0.025	0.204	-0.056	0.021
R^2	0.85		0.27	

*Table A2: Hierarchical partitioning for the multivariate regression models of the first two spatial patters (**sEOF1** and **sEOF2**) vs. both atmospheric parameters & land use components*

Model Formula : EOF.. ~ wsnc + spe + tke + Lwemitted + dm + xx + h + l + sd + s + kg + p

	Paramter	Abbv.	EOF_1 Explained Variance - R^2		EOF_2 Explained Variance - R^2		EOF_3 Explained Variance - R^2	
Atmospheric Parameters	A5- WindSpeed	wsnc	9	68	5	27	5	42
	A12- SpecHumidity	spe	34		11		24	
	A14- Turbulent Kinetic Energy	tke	22		5		7	
	S21-Surface Longwave Emitted Radiation	Lwemitted	3		7		6	
Land use Parameters	Trees	dm	1	32	4	73	2	58
	Grass	xx	2		6		10	
	Hedges	h	12		4		13	
	Loamy Soil	l	6		5		8	
	Sandy Soil	sd	5		31		17	
	Asphalt	s	3		14		4	
	Yellow Bricks	kg	1		4		2	
	Concrete Pavement	p	2		5		2	
	Sum All R^2		100	100	100	100	100	100